Creep detection of Hastelloy X material for gas turbine components with nonlinear ultrasonic frequency modulation

Frank Mevissen and Michele Meo *

Materials Research Centre, Department of Mechanical Engineering,

University of Bath, Bath, BA2 7AY, UK

E-mail: f.mevissen@bath.ac.uk, * Correspondence: m.meo@bath.ac.uk

Abstract

Creep damage is one of the main failure modes in hot-gas-leading components in gas turbines, which results from high temperatures along with mechanical loads. The aim of this study is to clarify the metallurgical creep behaviour of the Hastelloy X material and detect and evaluate creep damage at an early stage with a nonlinear ultrasonic modulation technique.

For this purpose, multiple samples were examined to demonstrate that pores and microcracks in grain boundaries spread from the outside to the inside. Inside the specimen, molybdenum was identified as the main precipitation element. In addition, the chromium diffusion in the outer areas led to the depletion of this element and favoured the formation of pores and microcracks. Failures were proven with nonlinear dual-frequency ultrasound technology. Moreover, two different longitudinal waves were sent into the samples to use harmonic and modulated response frequencies for evaluation. As a result, harmonic frequencies offered a favourable prediction of pore sizes, whereas defined sideband frequencies reacted very sensitively to the damage density and area distribution of the failures.

This study offers a method for detecting creep damage with nonlinear ultrasound techniques at an early stage as well as for differentiating between pores, microcracks, dislocations and precipitation. Therefore, the design of future gas turbine components made of Hastelloy X can be adapted with regard to the shown metallurgical behaviour and damage signatures.

1. Introduction

In modern gas turbines, it is important for the turbine blades and other hot-gas-leading components to be able to withstand extreme loads. Such loads include not only high centrifugal and gas forces, but also high temperatures. Since these high-tech components are challenging to manufacture, the goal is to extend their lifetime as much as possible. To assess the mechanical integrity of these parts, appropriate test technologies are required for the various failure modes. As a result of the continuous mechanical load on gas turbines used for power generation, coupled with the high temperatures, creep and oxidation commonly occur as failure modes [1], which can even lead to component failure.

In general, creep damage begins after a component is exposed to a high mechanical load and temperature, resulting in elastic strain. This is then followed by the primary stage, at which the strain rate decreases to a constant creep rate. The secondary stage of creep is usually

characterised by a slow but constant plastic flow of material. Then, during the tertiary stage, additional pores form and the strain further increases, ultimately leading to component failure [2].

To detect these failures at the earliest stage possible, various technological approaches have been developed. For example, in [3], Semenov et al. investigated the crack growth kinetics of fatigue, creep and thermal fatigue cracks in turbine blades. In addition, in [4], Chen et al. made a lifetime prediction of turbine blades under creep. Moreover, in [5], using the Larson–Miller parameter, Marahleh et al. investigated the possibility of a numerical assessment of the service life of turbine blades with creep load. In [6], Kim et al. estimated the material deterioration of high-temperature components. Maharaj et al. studied the finite element simulation of creep behaviour at the coupling of a turbine blade to a turbine disc in a fir-tree region [7]. Lui et al. investigated a turbine blade failure due to creep [8] and proposed a numerical approach for assessing the service life of turbine blades, which is based on the Lemaitre–Chaboche creep damage model. Shi et al. studied an experimental method for the determination of creep with low cycle fatigue [9]. Hyde et al. used finite element methods based on Norton's creep law to predict the creep life of pipes [10]. Finally, in a review study, Raj et al. described and evaluated existing material characterisation techniques [11].

Another promising area is the use of nonlinear ultrasound techniques. For example, Baby et al. used a second-order nonlinearity parameter to detect creep [12] and assess service life. They found that the nonlinearity parameter (β) increases until reaching a maximum value at creep fraction life of ~0.6 and then decreases again until the test component breaks. Balasubramaniam et al. described a new nonlinear ultrasound technique for characterising creep damage [13]. They assessed the nonlinear response of samples at much lower amplitudes than those used in previous studies on nonlinear material behaviour. They also successfully detected creep damage to welded steel pipes with nonlinear ultrasound using the second harmonic nonlinearity parameter [14]. However, in their case, the weld seam did not lead to an increase in nonlinearity. Kang et al. compared different studies on creep und mechanical plastic deformation with second- and third-order nonlinearity parameters [15]. In another study, Xiang et al. examined titanium alloys with nonlinear Lamb waves. Because of the dispersive behaviour of Lamb waves, they performed phase synchronisation in the dispersion diagram so that both the fundamental and the harmonic frequencies move with the same phase velocity. They found

that the initial creep load increases the level of nonlinearity as a result of the precipitation and dislocation effect. Since these factors decrease with higher creep loads, resulting in the generation of additional voids, the level of nonlinearity decreases [16]. In another study, a new analytical model was presented, which combines the wave equation of nonlinear Lamb waves in a plate with a dislocation model [17, 18]. The study results showed that the precipitation–displacement interaction has the greatest influence on the change in the second-order nonlinearity during creep in materials. Valluri et al. described a technique for characterising creep damage using nonlinear ultrasound, wherein the third harmonic nonlinearity parameter is the most sensitive [19]. Other researchers have also highlighted that high operating temperatures lead to increased oxidation, which can cause material failure as a result of the reduced functional properties of oxides [1, 20–22].

In this study, a frequency modulation excitation concept is proposed to detect creep damage in gas turbine materials. Three different creep samples were examined, two of which were identically loaded. The only difference between these two samples is that one of them was welded at the middle. The third sample was loaded with a higher temperature but with a lower tensile force. To obtain a metallurgical classification, the damage size, damage density and area distribution of the pores were evaluated. The primary precipitation element was identified using the characteristic X-ray radiation of a scanning electron microscope. This technique is used for the detection of cracks [23, 24] and the determination of plastic deformation [25], two failure modes that also occur in the case of creep damage. Finally, the measured amplitudes and calculated nonlinearity parameters were compared with the metallurgical data.

2. Specimen

The creep samples were made of a material called Hastelloy X (DIN designations: No. 2.4665 and NiCr22Fe18Mo). This material is highly resistant to oxidation and is, therefore, often used in the hot-gas-leading parts of gas turbines. Its chemical composition is shown in Table 1.

Table 1. Nominal chemical composition [m%] of Hastelloy X [26].

Ni	Cr	Fe	Mo	Co	W	C	Mn	Si	B
47	22	18	9	1.5	0.6	0.1	1	1	0.008

The samples had dimensions of 2 × 30 × 150 mm. Figure 1a illustrates the unloaded reference sample from the same batch, which was used for comparison. All creep samples had measuring tips that were used for continuous strain measurement during the creep tests. Sample CR2-1 was

broken after 3250 h and loaded with 70 MPa and 750 °C (Figure 1b), and a strain of 6.3% was achieved. Sample CR2-2 (Figure 1c) was loaded with identical parameters but was welded at the middle to assess the influence of the weld seam on the creep behaviour. Sample CR3 was loaded with 35 MPa and 800 °C for 5850 h (Figure 1d), and a strain of 1% was reached before the test was stopped.

Figure 1. Creep specimens: (a) CR1; (b) CR2-1; (c) CR2-2; (d) CR3.

Figure 2 shows that widely different strain values were measured for samples CR2-1 and CR2-2. In sample CR2-2, a slightly higher strain than that in sample CR2-1 was determined up to 580 h. However, after that, the values plateaued and sample CR2-1 showed a significantly greater strain, leading to the breaking of the sample at 3250 h. For the welded sample CR2-2, the tests were stopped after 3200 h when a strain of 2.5% was reached.

Sample CR3 was loaded with 800 °C and 35 MPa for 5900 h. When the strain reached 1%, the tests were also stopped.

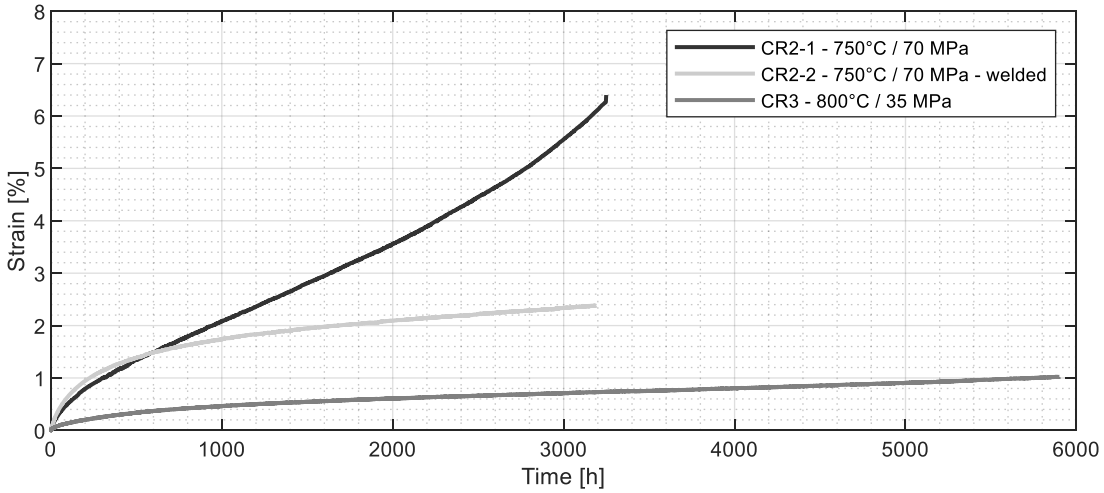

Figure 2. Strain–time diagram of creep samples.

Table 2 provides an overview of the samples used along with the test parameters and resulting strain values.

Table 2. Experimental parameters of the creep test.

Specimen	Temperature [°C]	Load [MPa]	Time [h]	Strain A [%]
CR2-1	750	70	3250	6.3
CR2-2 (welded)	750	70	3200	2.5
CR3	800	35	5850	1.0

3. Metallurgical Evaluations

To investigate the level of damage, the samples were metallurgically examined. First, to prepare for the metallurgical studies, the samples were ground to 0.5 mm. Then, one section plane was examined with the assumption that the statistical failure distribution of the entire plate samples with small wall thicknesses is comparable. These sample elements were then embedded in a plastic mould (Figure 3) to facilitate the following grinding and polishing work. To examine the cracks more closely, sample CR2-1 was divided into two parts (Figure 3b).

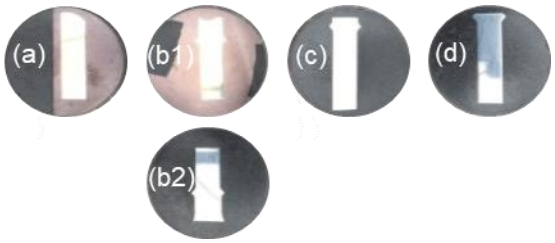

Figure 3. Sample preparation: (a) CR1; (b) CR2-1; (c) CR2-2; (d) CR3.

As outlined in Section 3.1, the samples were examined using a reflected light microscope (RLM). To make the grain structure visible, the samples were etched and then examined using a scanning electron microscope (SEM), as shown in Section 3.2. Finally, as shown in Section 3.3, the precipitation examinations were evaluated.

3.1. Reflected light microscopy

First, sample CR1 (reference sample) was investigated in different positions. The red dot shown in Figure 4 represents the position of an exemplary evaluation. From the figure, it can be seen that, apart from small carbide inclusions, no pores are visible.

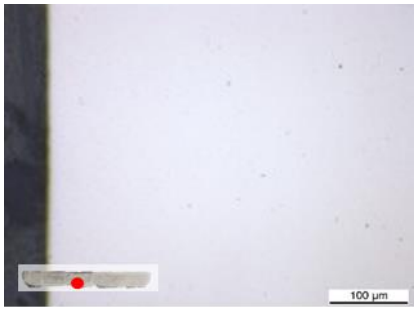

Figure 4. Reflected light microscopy of CR1.

As shown in Figure 5a, sample CR2-1 exhibited a crack area with enormous damage in the base material. Moreover, as shown in Figure 5b, approximately 5 mm away from the crack, a large number of pores and microcracks were detected. Figure 5c shows the area of the transition radius to the measuring tip. As shown in Figure 5d, the higher pore density was due to the influence of the breaking area. This influence then decreased (see Figure 5e and Figure 5f), and the damage was mainly revealed at the side areas.

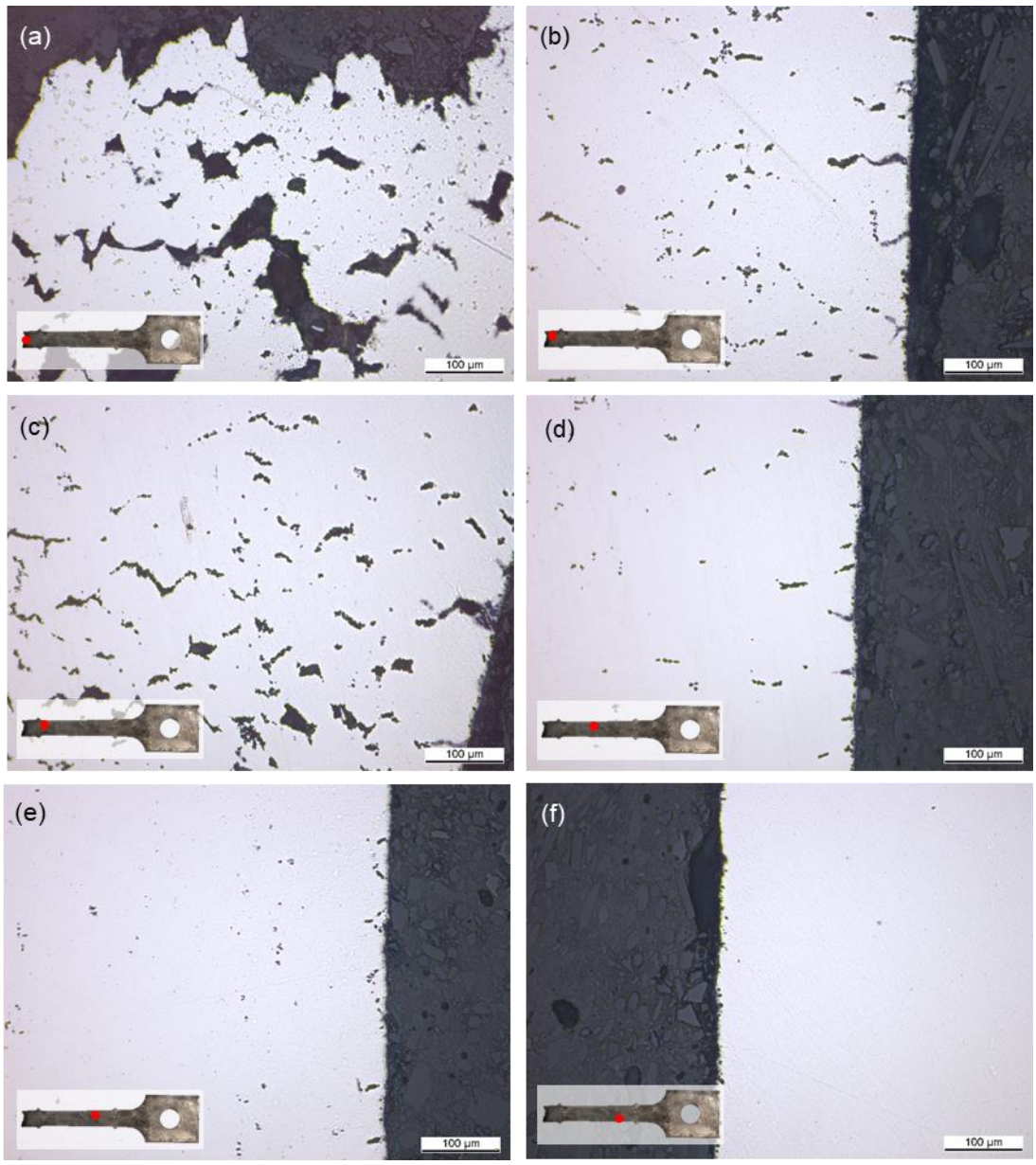

Figure 5. Reflected light microscopy of CR2-1.

Compared to the identically loaded sample CR2-1, stronger formation of microcracks was visible for sample CR2-2, with a length reaching up to 100 µm (Figure 6). However, no difference between the weld seam area and the rest of the material was determined. In [14], no influence of creep damage on weld seam was found either. The area of the transition radius showed pronounced microcracks (Figure 6d).

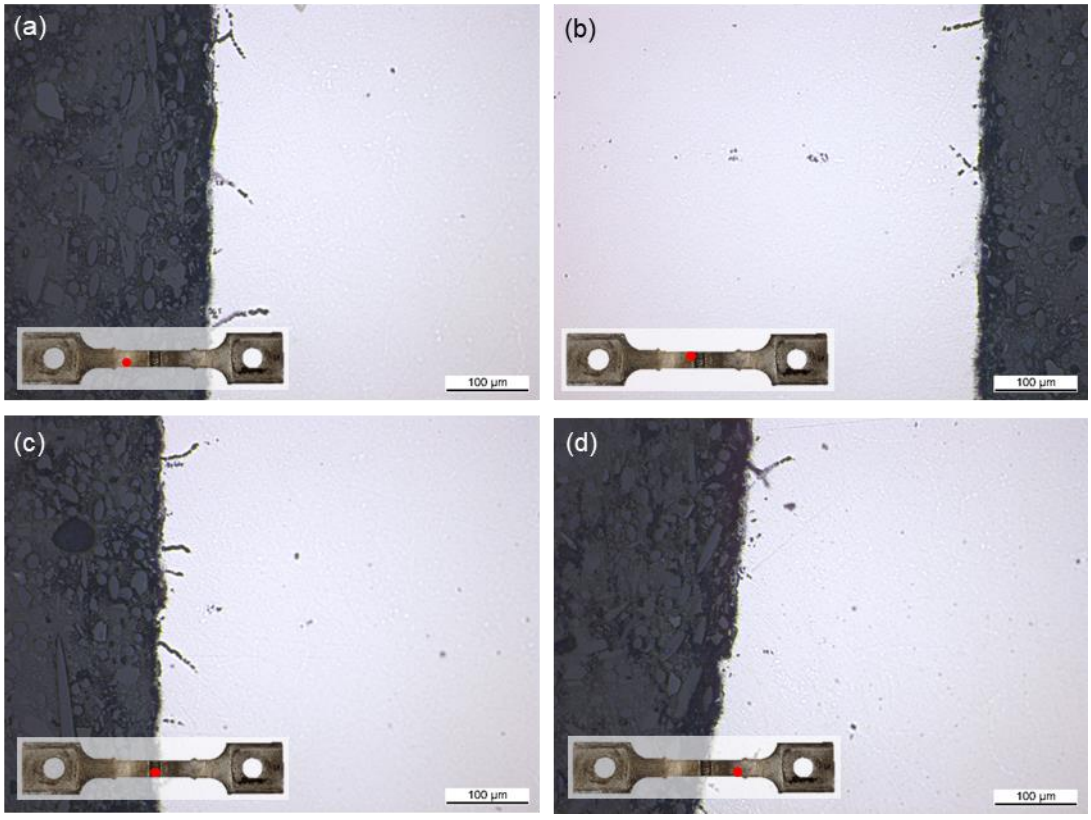

Figure 6. Reflected light microscopy of CR2-2.

Figure 7 shows the analysis results of creep damage in sample CR3. From the figure, it is clear that the damage progressed from the outside to the inside. Many small pores were visible in the edge area, which combined to form microcracks. In addition, a large concentration of imperfections were observed in the area of the transition radius (Figure 7d).

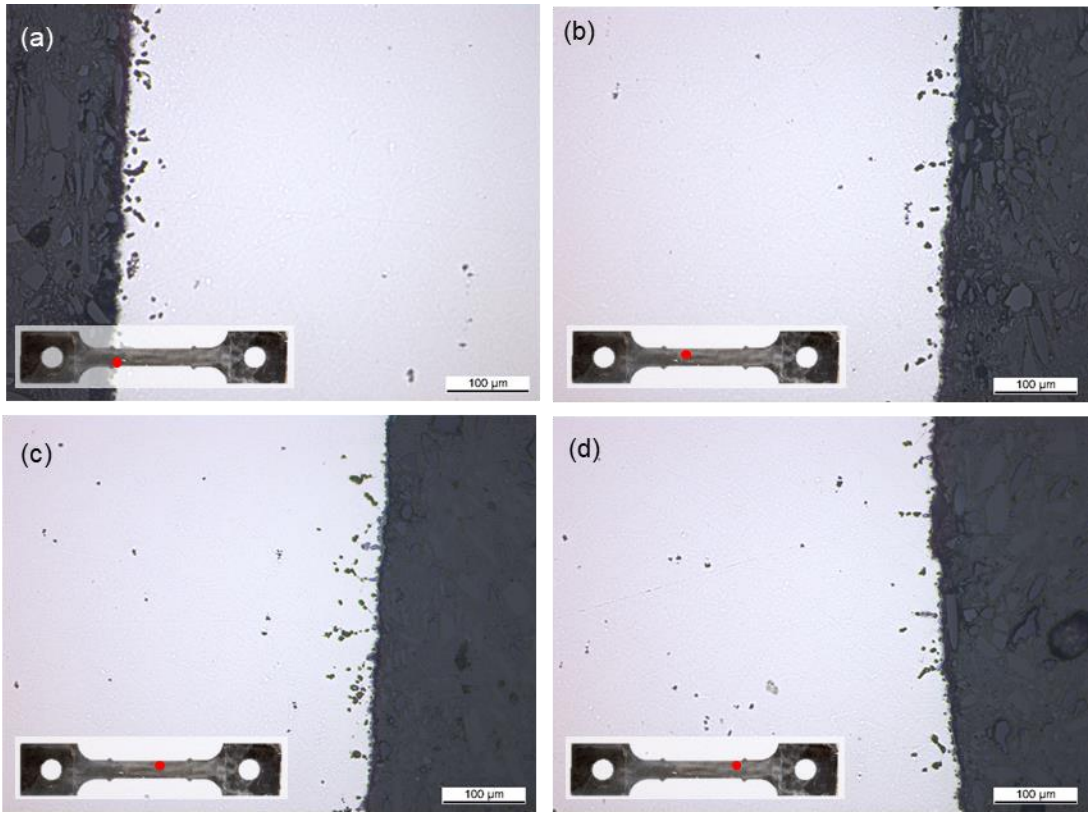

Figure 7. Reflected light microscopy of CR3.

The metallurgical results were evaluated in more detail using the image processing software Imagic IMS (Imagic Imaging Ltd., UK). The defect areas were statistically evaluated via colour mapping (Figure 8). Then, the damage sizes and the failure areas were evaluated.

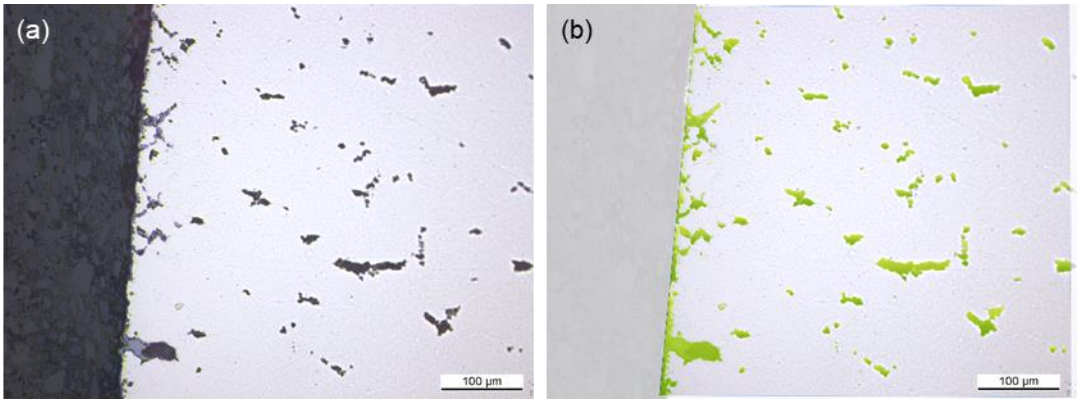

Figure 8. Surface evaluation: (a) original, (b) surface analysis.

Generally, the selection of areas to be evaluated is decisive for a meaningful evaluation. Therefore, the following evaluations were made:

- All evaluations between the measuring tips (A_{ALL}) (Figure 9a)

- Defined areas without the influence of breakage, weld seam and transition radius (A_D) (Figure 9b)
- Fillet radius areas (A_{FR}) (Figure 9c)

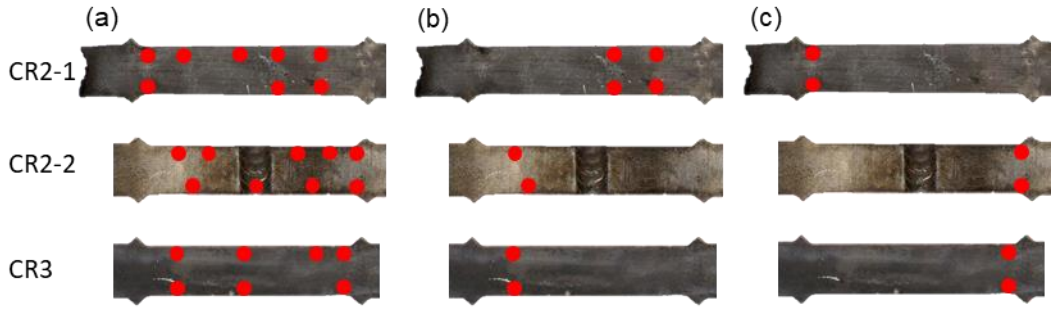

Figure 9. Evaluation areas: (a) A_{ALL}; (b) A_D; (c) A_{FR}.

From the images, the mean values of the damage sizes ($\bar{S}_d$) of individual samples were first determined (Figure 10a) and found to vary from 2.5 to 19.3 µm. In general, damage size is considered a good indicator for determining the current creep phase. Pores form first at the grain boundaries, which then combine to form microcracks and then progress to larger failures. With all values (A_{ALL}) considered, CR2-1 and CR2-2 show almost identical damage sizes, with the CR3 sample exhibiting the largest flaws. With the defined areas (A_D), the welded CR2-2 sample was found to have significantly larger pores than those of the broken CR2-1 sample. This was also demonstrated in the scanning electron microscopy images, wherein the pores in the edge area have already combined to form microcracks (Figure 6). Sample CR3 clearly showed the largest flaws, and sample CR2-1 had the largest damage in the transition radii.

Damage density (Figure 10b) describes the number of defects in an evaluated area and is calculated as $\rho_d = \frac{n_d}{A_0}$, where A_0 is the total evaluated area and n_d is the total number of damage points in the evaluation area. If several pores connect to form microcracks, this results in larger damage and a reduced damage density, hence further increasing the formation of pores in other positions. With all areas (A_{ALL}) and defined areas (A_D) considered, CR2-1 provided the highest density as a result of the influence of the break point of the sample. However, with only the transition radii considered, sample CR3 had the highest values.

In an area-based evaluation, the values are provided as percentages (Figure 10c). Sample CR2-1 exhibited peak values when all the values and the values at the transition radii were considered: $A_R = \frac{A_{\sum d} \cdot 100}{A_0}$, where $A_{\sum d}$ is the total area of damage. With the defined areas (A_D)

considered, the values increased steadily from sample CR2-1 to sample CR3. This sample was loaded the longest, for a total of 5850 h.

When the damage density (ρ_d) and area proportion (A_R) reached a critical value, the remaining cross section became unable to withstand the load and the component failed.

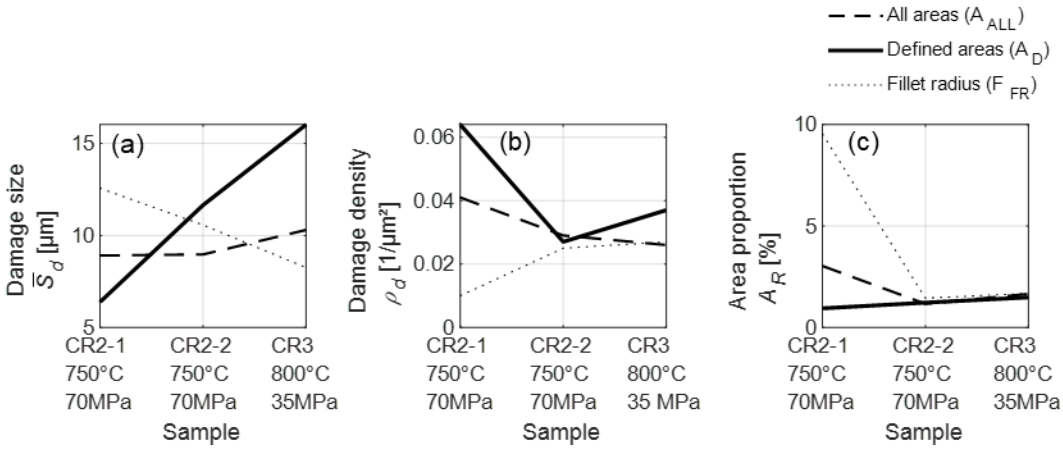

Figure 10. Metallurgical evaluation: (a) damage size; (b) damage density; (c) area proportion.

3.2. Scanning electron microscopy

To evaluate the influence of creep damage on the microstructure, the etched samples were examined using a scanning electron microscope. Figure 11 shows the reference sample with a clear austenitic crystalline structure with primary carbides, which formed during the solidification of the melt.

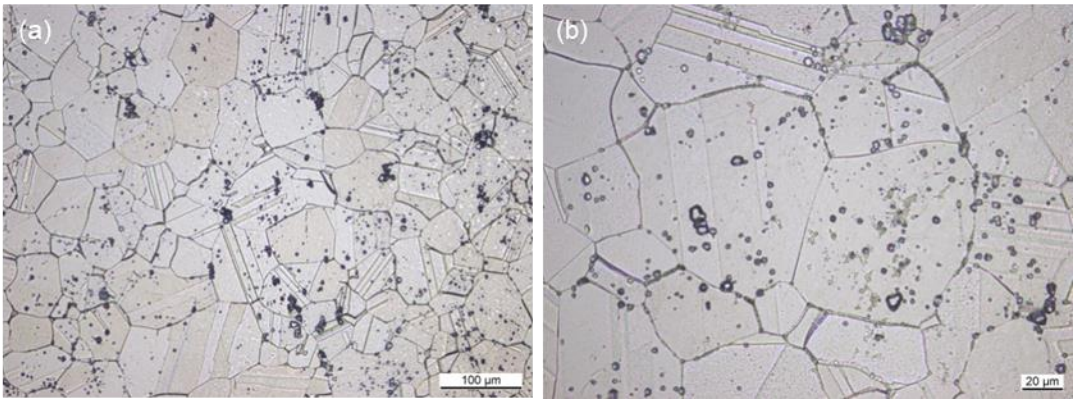

Figure 11. Scanning electron microscopy images of sample CR1.

Although sample CR2-1 (Figure 12) shows an austenitic structure, a high precipitation density can also be observed, with occasional pore formation at the grain boundaries.

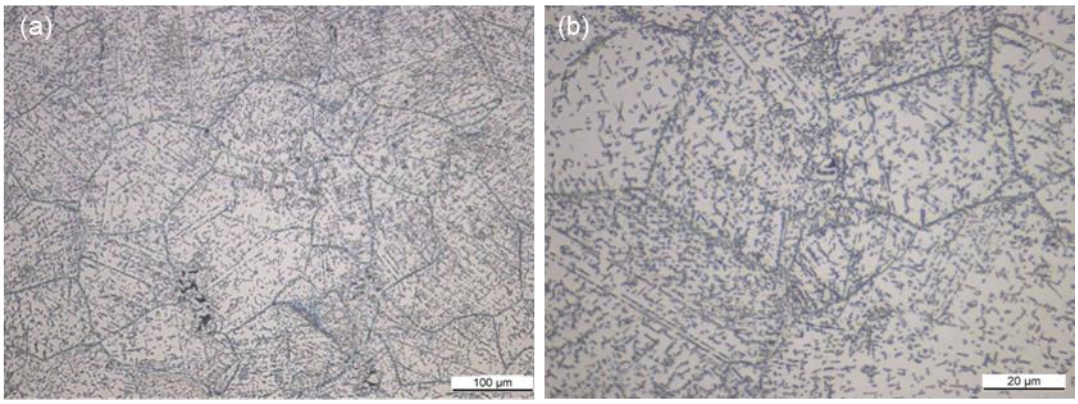

Figure 12. Scanning electron microscopy images of sample CR2-1.

In addition to an increased precipitation density, the welded CR2-2 sample was found to exhibit clear microcracks on the sides (Figure 13). The pores inside were hardly detectable, and there was no discernible difference in the welded area (Figure 13a).

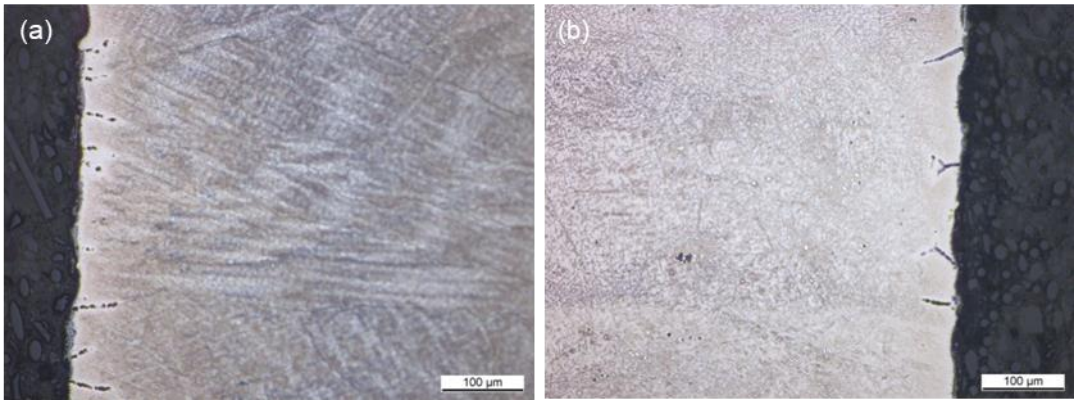

Figure 13. Scanning electron microscopy images of sample CR2-2.

Sample CR3 demonstrates how creep damage develops. In Figure 14a, an oxide layer can be observed on the outside, from which the creep damage progresses. Moreover, for this sample, pores form at the grain boundaries from the outside to the inside, which then combine to form microcracks at points with a high precipitation density.

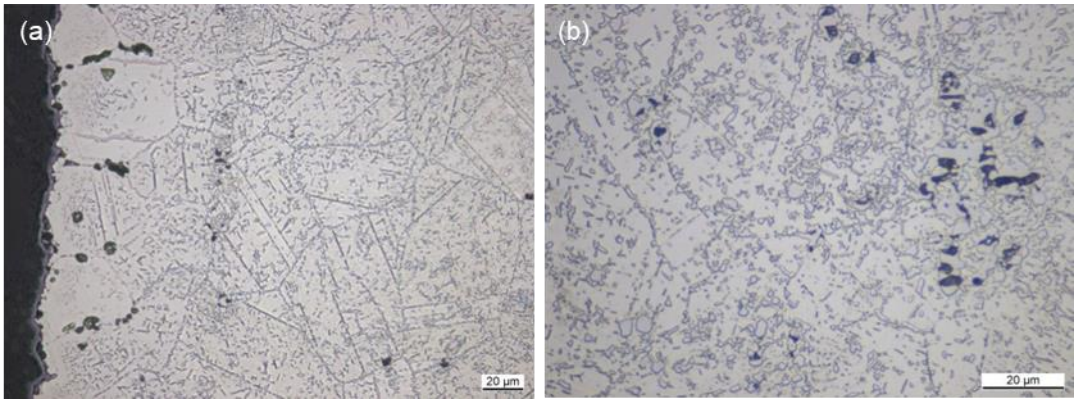

Figure 14. Scanning electron microscopy images of sample CR3.

3.3. Precipitation

With a scanning electron microscope, an increased precipitation density was detected in all creep samples. This section focusses on determining which elements are mainly involved in precipitation.

Characteristic X-ray radiation was used along with SEM and energy-dispersive X-ray (EDX) analysis to characterise element precipitation in creep samples. Figure 15 illustrates the mapping inside the specimen. Analysis showed that molybdenum was the primary precipitation element, and nickel the secondary precipitation element.

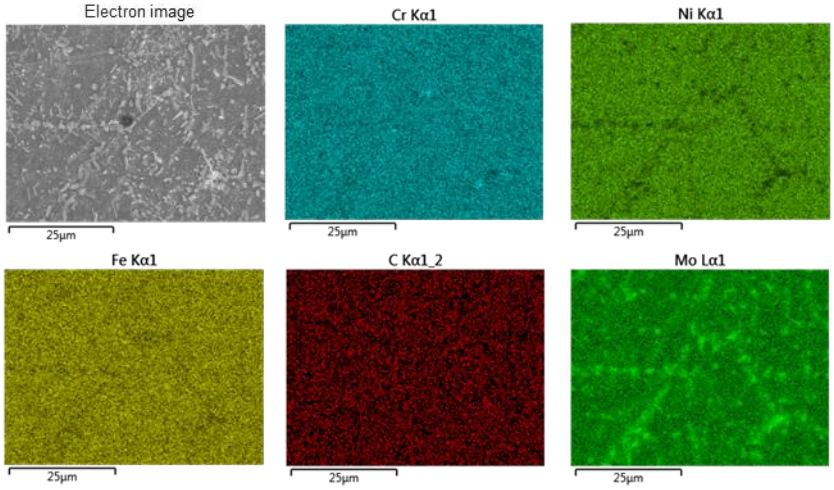

Figure 15. EDX mapping of the inner area.

Figure 16 shows the element mapping at the edge of a sample, where intergranular microcracks have already formed. It can be observed that chromium mainly diffused outwards into the edge area, where oxygen was also found to exhibit an increased concentration. Comparison of the chromium and oxygen mapping revealed the formation of chromium oxide in the edge area,

which led to the depletion of chromium inside. In the case of nickel and iron, only a few dislocations formed in the outer oxide layer. However, molybdenum showed no dislocations in the edge area.

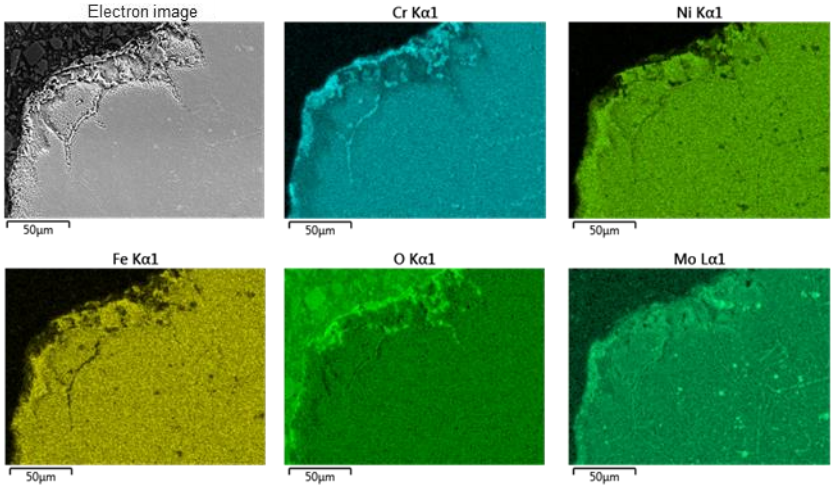

Figure 16. EDX mapping of the outer area (crack).

Because of the temperature load, the chromium particles diffused out of the mixed crystal as a result of their high affinity for oxygen, where they oxidised directly outside the material [22]. If no natural oxide is present on the surface, then the process of oxidation starts with the adsorption of oxygen on the surface, followed by the splitting of O_2 atoms into O atoms. Then, as the reaction proceeds, oxygen is dissolved in the metal and an oxide is formed.

Overall, since the carbides in the area near the edge are also dissolved, this leads to a certain degree of harmonisation. The reaction occurs at both the metal–oxide and the oxide–oxygen interfaces, forming several oxide layers [22]. Above 900 °C, the oxide layers evaporate over a long period of time. Therefore, the chromium oxide needs to be reproduced repeatedly from the metallic chromium present in the base material. Figure 17 shows a chromium(III) oxide layer (Cr_2O_3), which is very hard and brittle. The typical corundum crystalline structure consists of hexagonal lattices.

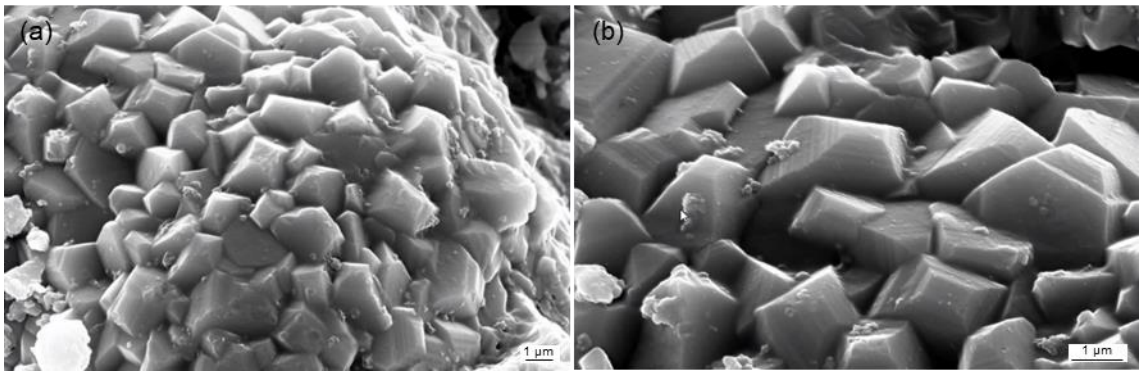

Figure 17. Chromium(III) oxide (Cr_2O_3): (a) overview; (b) crystal structure.

Figure 18a shows another representative sample in which a second layer of iron/nickel oxide has formed on the chromium oxide layer, represented as a red line in the EDX image (Figure 18b). However, the level of adhesion was found to be significantly lower than that of the chromium oxide layer.

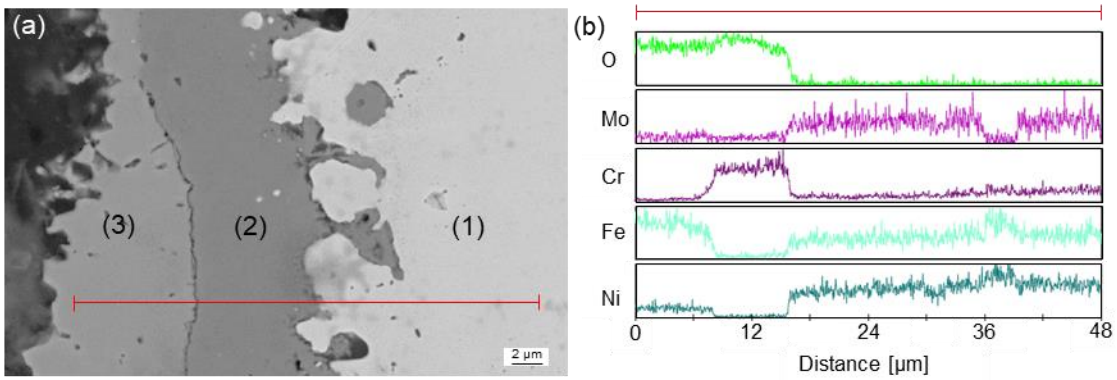

Figure 18. Oxide layer: (a) (1) base material, (2) chromium oxide and (3) iron/nickel oxide; (b) concentration profile, EDX analysis.

According to the level of damage, pores form at the grain boundaries of edge areas as a result of chromium diffusion. In this area, the concentration of the base material depletes in chromium over time. Therefore, its concentration falls below a critical level and internal oxidation and subsequent material failure occur [27]. It is also worth noting that creep damage favours the formation of intergranular pores and cracks, resulting in mixed damage from oxidation and creep.

4. Ultrasonic Experiments

Before the samples were prepared for the metallurgical tests, they were examined with longitudinal ultrasound waves. Then, the measured amplitudes of the different frequencies were

used to evaluate the measurement results. Generally, an introduced ultrasonic wave propagates in a body with a defined frequency. If this propagation is disturbed as a result of a failure, harmonic frequencies are produced [28–33]. The amplitudes of these harmonic frequencies are then measured and compared to those of the fundamental frequencies. Using two fundamental frequencies has been proven to be an indicator for the detection of material changes with a high resolution [23, 24]. Dual-frequency excitation not only delivers harmonic frequencies for each excitation frequency but also interdependent modulated response frequencies. The following expressions show the nonlinearity parameters used to evaluate the ultrasonic experiments in this study [23, 24]:

$$\begin{aligned}
\beta_{2f1} &\propto \frac{A_{f1+f2}}{{A_1}^2}, \\
\beta_{2f2} &\propto \frac{A_{f1+f2}}{{A_2}^2}, \\
\gamma_{3f1} &\propto \frac{A_{f1+f2}}{{A_1}^3}, \\
\gamma_{3f2} &\propto \frac{A_{f1+f2}}{{A_2}^3}, \\
\beta_{f2\pm f1} &\propto \frac{A_{f1+f2}}{A_1 A_2}, \\
\gamma_{2f1\pm f2} &\propto \frac{A_{f1+f2}}{{A_1}^2 A_2}, \\
\gamma_{2f2\pm f1} &\propto \frac{A_{f1+f2}}{A_1 {A_2}^2}.
\end{aligned} \tag{1}$$

The criteria for the selection of fundamental frequencies are as follows:

- No frequency overlap $\left(f2 \neq \frac{f1}{2}\right)$
- Positive frequency values $\left(f2 > \frac{f1}{2}\right)$
- Sensor bandwidth

Table 3 shows the frequencies evaluated with the chosen excitation frequencies (f_1 = 6 MHz, f_2 = 10 MHz) covering a harmonic and sideband frequency range from 2 to 30 MHz.

Table 3: Evaluated frequencies.

Fundamental/harmonic/ sideband	Frequency [MHz]
f_1	6
f_2	10
$2f_1$	12
$2f_2$	20
$3f_1$	18
$3f_2$	30
f_2+f_1	16
f_2-f_1	4
$2f_1+f_2$	22
$2f_1-f_2$	2
$2f_2+f_1$	26
$2f_2-f_1$	14

4.1. Experimental setup and procedure

In this study, a Rigol DG1022Z pulse generator was used to generate the frequencies. Two frequencies (i.e. $f_1 = 6$ MHz, $f_2 = 10$ MHz) were sent over two channels to a Falco WMA-300 amplifier and amplified with an output voltage of 150 V. The signals were sent to the sample by Sensor S, and the longitudinal waves were received on the other side with Sensor R and amplified with a Phoenix ISL 40 dB amplifier. Olympus V129-sm contact transducers were used for this application. The measurement data were then sent to an oscilloscope for further processing. A total of 100 pulses were sent, and their mean values were considered. This not only allowed avoiding wave reflections but also increased the probability of passing small flaws. The wave propagation due to the reduced wall thicknesses of the deformed components was examined without any influence [25]. In the additively manufactured specimen-clamping and positioning device shown in Figure 19b, the sample can be moved around two axes with a constant sensor position.

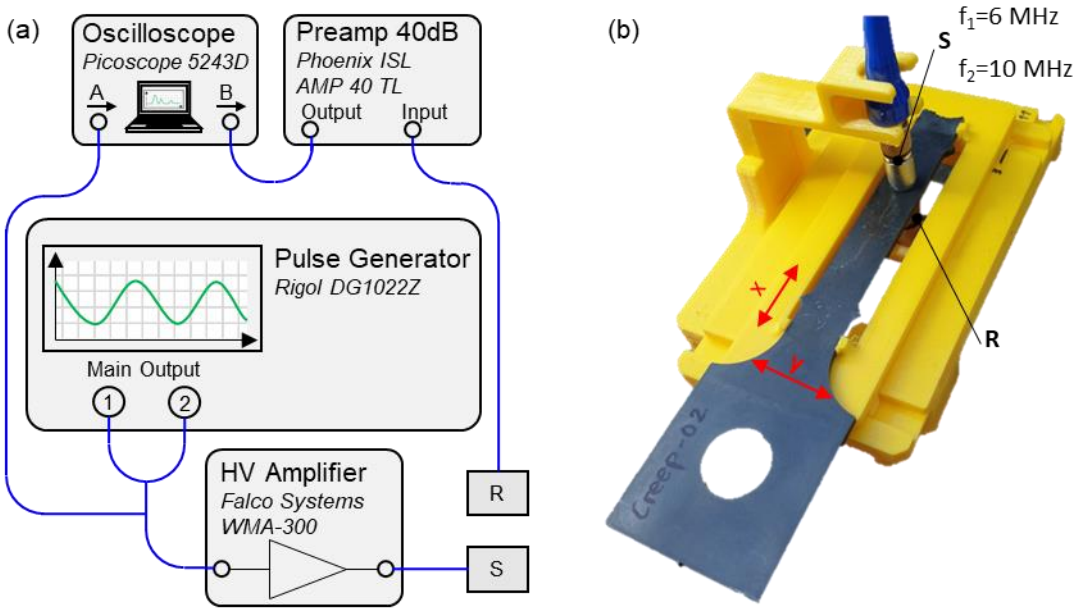

Figure 19. Experimental setup: (a) overview; (b) sensor attachment to a sample.

The area between the measuring tips was first examined (Figure 20), and then 3 × 21 measuring points were documented in the area between the strain measuring tips. Figure 20 shows the grid of the measuring points of the examined vertical rows (R1 to R3) and horizontal columns (C1 to C21).

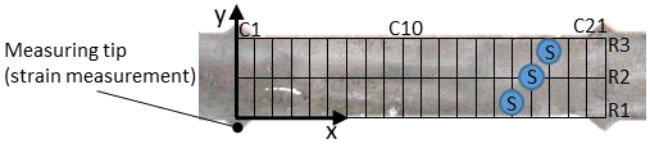

Figure 20. Experimental procedure.

4.2. Experimental results

The measurement results are shown in Figure 21–Figure 23 as calculated contour plots. The same legend scaling was used for all samples for the respective nonlinearity parameters.

Figure 21a,b illustrate the evaluations of the second harmonic frequencies ($2f_{1,2}$), revealing an increase in the nonlinearity parameters compared to the reference sample. Increased nonlinearities were also detected in the area of the fracture, which extended into the sample approximately 10 mm from the measuring tips. With the parameter of frequency $2f_1$, increased nonlinearities were also detected at the transition radii to the measuring tips. This evaluation revealed higher parameter values in the side areas along the *x*-axis compared to the middle. The third harmonic frequencies were also found to behave similarly (Figure 21c,d), and the creep

damage was clearly observed. Moreover, the values in the middle area were slightly lower than on the sides.

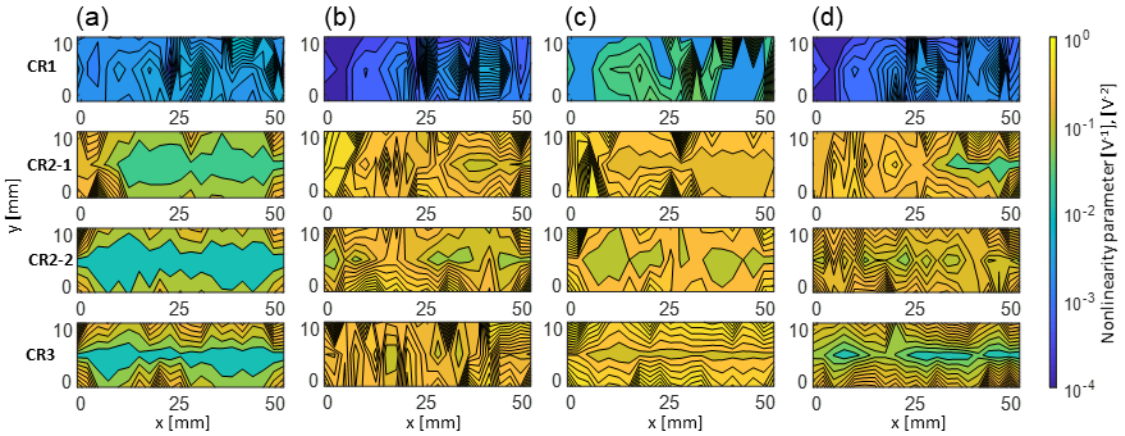

Figure 21. Nonlinearity parameters: (a) $2f_1$; (b) $2f_2$; (c) $3f_1$; (d) $3f_2$.

Overall, the first sideband frequencies ($f_2 \pm f_1$) exhibited partly opposite behaviour. In contrast to the f_2+f_1 frequency (Figure 22b), the middle range was smaller at the f_2-f_1 frequency (Figure 22a). The zone of influence of the fracture can be clearly observed in both figures.

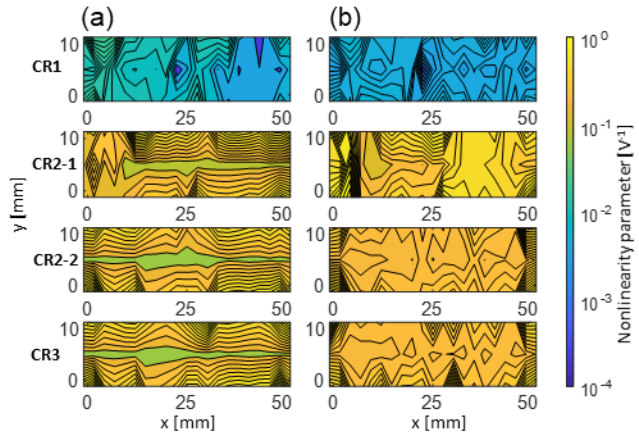

Figure 22. Nonlinearity parameters: (a) f_2-f_1; (b) f_2+f_1.

In general, the contour plot of the $2f_1 \pm f_2$ frequency illustrates the different characteristics of the middle area (Figure 23a,b). Increased nonlinearities were also observed at the corners, especially for the $2f_1-f_2$ frequency.

Overall, the previously determined behaviour continued for the sideband frequency $2f_2 \pm f_1$ (Figure 23c,d). Moreover, the middle ranges of the $2f_2-f_1$ frequency were clearly more pronounced than with $2f_2+f_1$, and the zone of influence of the crack was identified with the

sidebands. The corner areas, where the transition radii to the measuring tips were positioned, also showed increased nonlinearity values.

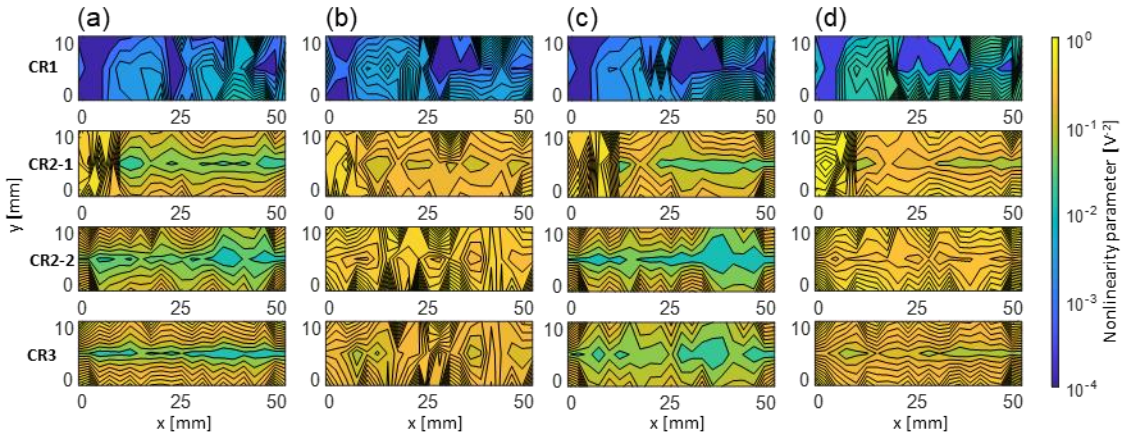

Figure 23. Nonlinearity parameters: (a) $2f_1-f_2$; (b) $2f_1+f_2$; (c) $2f_2-f_1$; (d) $2f_2+f_1$.

In summary, nonlinear ultrasound techniques with dual-frequency excitation were used to clearly identify the creep damage and crack zone in CR2-1. It was also observed that the $2f_1-f_2$ and $2f_2-f_1$ frequencies behave differently in the middle range compared to the $2f_1+f_2$ and $2f_2+f_1$ frequencies. In addition, increased nonlinearities were measured in the area of the transition radii. However, tests with removed oxide layers did not yield different results.

5. Results and discussion

In Section 3, we showed that the formation of pores begins at the outward grain boundaries, which then combine to form microcracks when the level of creep loading is increased. Although there were hardly any pores inside the material, the precipitation density was very pronounced. The ultrasonic measurements showed that pores and microcracks with sizes from 6.4 to 16 µm can be detected.

Moreover, the ultrasound test outlined in Section 3 revealed a difference in the measured data. Figure 24 shows a sectional image of a sample with metallurgical defects. The outer part is surrounded by oxide layers followed by pores and microcracks, and the inside part contains dislocations and precipitations. When measurements were performed in the middle (R2), the pores and microcracks on the top and bottom were found to lead to the formation of increased nonlinearities. In addition, measurements in the edge areas (R1 and R3) showed that the ultrasonic waves passed the pores and microcracks in the top, bottom and side areas. This difference is demonstrated in the contour plots in Section 4.2.

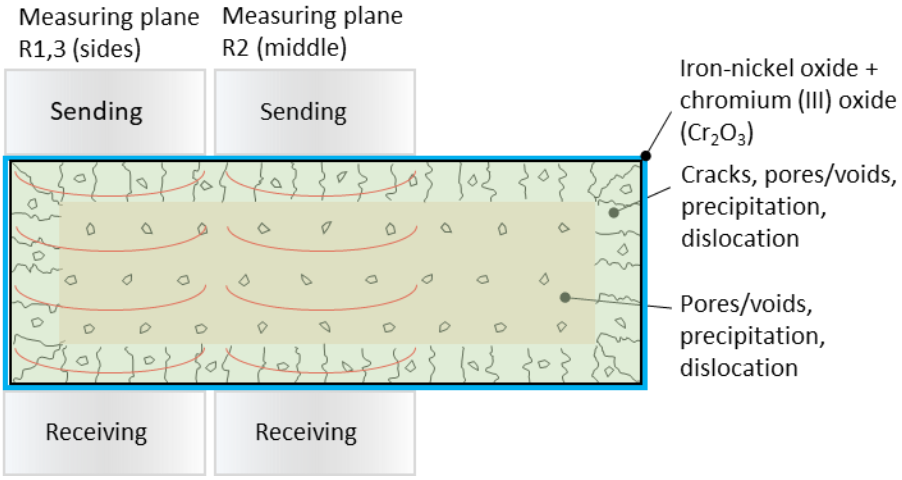

Figure 24. Sectional image of a sample undergoing an ultrasonic measurement.

A difference between the $2f_1-f_2$ and $2f_2-f_1$ nonlinearity parameters and the $2f_1+f_2$ and $2f_2+f_1$ nonlinearity parameters was also observed. This phenomenon has been demonstrated in material plasticity [25], in which the dislocation theory was combined with a one-dimensional wave equation with dual-frequency excitation. Table 4 shows the behaviour of the individual harmonic and modulated response frequencies, which have been analytically and experimentally proven.

Table 4. Dislocation behaviour [25].

Frequency	Behaviour nonlinearity parameter [1]
$2f_1$	–
$2f_2$	+
$3f_1$	–
$3f_2$	–
f_2-f_1	–
f_2+f_1	+
$2f_1-f_2$	–
$2f_1+f_2$	+
$2f_2-f_1$	–
$2f_2+f_1$	+

'+' means an increasing nonlinearity parameter with increasing plasticity.
'–' means a decreasing nonlinearity parameter with increasing plasticity.
[1] Measurement perpendicular to the surface and the tensile load vector.

Although the nonlinearities measured in [25] are considered evidence of dislocations in the material, the behaviour was not quite pronounced as in [25]. It was also found that the increased nonlinearities in the area of the transition radii are due to increased pore formation and microcracks.

Figure 25 shows a normalised comparison of nonlinearity parameters together with metallurgical data. For this study, A_{ALL}, A_D and A_{FR} were compared (Figure 9). For the sake of clarity, the harmonic nonlinearity parameters and sideband parameters were shown separately.

As shown in Figure 25a, sample CR2-1 had the greatest damage density and defect area, with the sideband frequencies showing a favourable match. In addition, sample CR3 exhibited the largest damage size, with the harmonic frequencies $2f_{1,2}$ and $3f_{1,2}$ reaching their peaks.

When A_D was considered (Figure 25b), the behaviour changed. For instance, CR2-1 had the largest damage density with the summing sidebands (i.e. f_2+f_1, $2f_1+f_2$ and $2f_2+f_1$), whereas CR3 had the largest area occupancy and damage size, with the harmonic frequencies $2f_{1,2}$ and $3f_{1,2}$ reaching their peaks.

During the radius evaluation (Figure 25c), sample CR2-1 was found to have the largest area occupancy as well as a relatively large damage density as a result of the influence of the fracture with the sideband frequencies f_2+f_1, $2f_1-f_2$ and $2f_2\pm f_1$. Moreover, sample CR3 was found to exhibit the largest damage size, which is also mirrored in the harmonic frequencies.

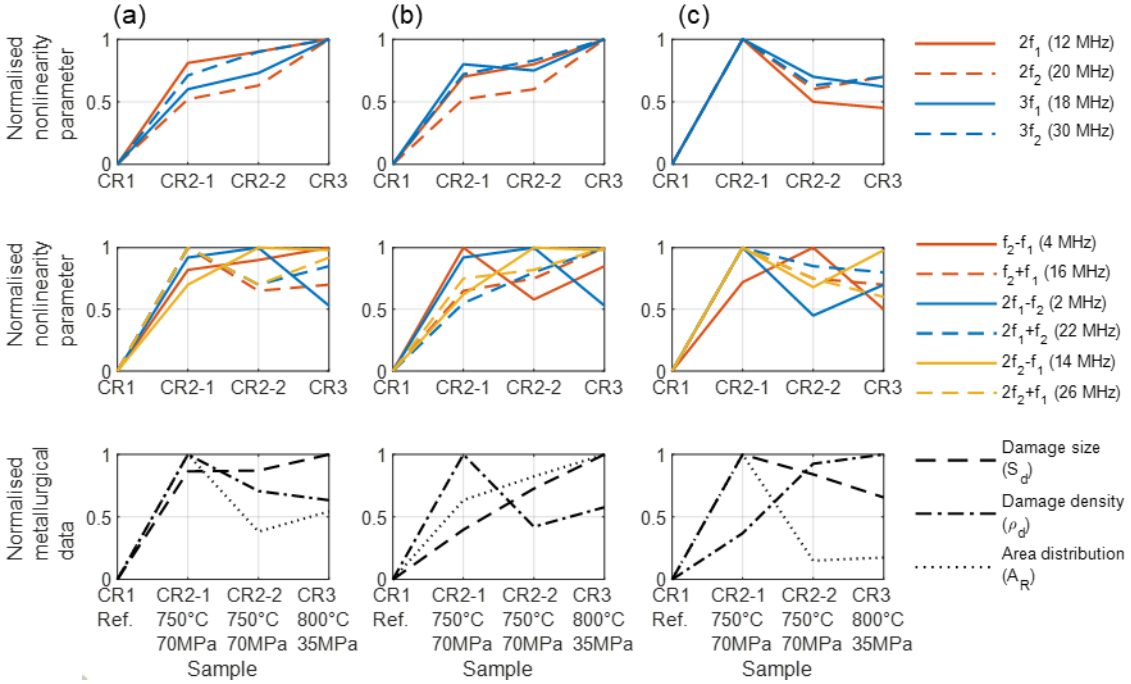

Figure 25. Comparison: (a) A_{ALL}; (b) A_D; (c) A_{FR}.

According to this evaluation, the harmonic frequencies $2f_{1,2}$ and $3f_{1,2}$ seem to be very sensitive to the size of the damage. With regard to the damage density and area, the summing

sideband frequencies f_2+f_1, $2f_1+f_2$ and $2f_2+f_1$ showed very favourable matches, along with comparatively high frequencies (16, 22 and 26 MHz).

Generally, the different strain behaviour of sample CR2-1 and the welded CR2-2 sample can be explained by the high constriction in sample CR2-1 and thus the higher strain, which, however, was not constant over the entire measuring distance. In Figure 2, it can be seen that the sample started undergoing a strong strain from 343 h onwards.

It can be assumed that the relatively large damage sizes of samples CR2-2 and CR3 are due to the pores being already connected to form microcracks (Figure 6 and Figure 13).

The oxidation resistance of Hastelloy X can be improved by applying a protective layer using MCrAlY [22]. In addition, creep damage can only be improved by reducing the mechanical load or reducing the temperature load, such as via active cooling.

6. Conclusion

In this study, we used a nonlinear modulation ultrasound approach to detect and image creep and oxidation damage in various samples made of Hastelloy X. Metallurgical investigations showed that it is possible to prove that the temperature load causes chromium to diffuse outwards in the edge areas of the samples to oxidise on the outside. Favoured by the lack of chromium in the edge areas, pores form at the grain boundaries, which then combine to form microcracks.

It was also found that the harmonic frequencies $2f_{1,2}$ and $3f_{1,2}$ can serve as a useful parameter to accurately measure the damage sizes of failures. Moreover, the modulated response frequencies f_2+f_1, $2f_1+f_2$ and $2f_2+f_1$ were found to be in good agreement with the total surface area of the pores and damage density. The dislocation theory was used to explain dislocations and precipitations in the material, allowing clear differentiation between dislocations and microcracks.

SEM analysis revealed a high dislocation density. It was also found that the weld seam exhibits the same creep damage as that in the base material. Moreover, EDX analysis identified molybdenum as the main precipitation element inside the material. In addition, the chromium diffusion at the edge areas led to the depletion of the element and favoured the formation of pores and microcracks due to intergranular corrosion.

Overall, the investigations presented herein offer a better understanding of creep damage in a material when it is used in gas turbines and also help in the design of hot-gas-leading

components. Nonlinear ultrasound technology has also been proven to be a powerful tool for detecting and classifying creep damage at an early stage as well as for differentiating between precipitation and microcracks.

Acknowledgement

Thanks to Wolfgang Bernauer, Dirk Formella and the MAN Energy Solutions SE for their support.

References

1. Mevissen, F., & Meo, M. (2019). A Review of NDT/Structural Health Monitoring Techniques for Hot Gas Components in Gas Turbines. *Sensors, 19*(3), 711.
2. Sahu, M. K., Swaminathan, J., Bandhoypadhyay, N. R., & Palit Sagar, S. (2018). Creep Damage Evaluation In P92 Steel Using Second Harmonic Of High Power Ultrasonic Signal. *Materials Today: Proceedings, 5*(2), 4467–4474.
3. Semenov, A. S., Semenov, S. G., & Getsov, L. B. (2015). Methods of Computational Determination of Growth Rates of Fatigue, Creep, and Thermal Fatigue Cracks in Poly- and Monocrystalline Blades of Gas Turbine Units. *Strength of Materials, 47*(2), 268–290.
4. Chen, L., Liu, Y., & Xie, L. (2007). Power-exponent function model for low-cycle fatigue life prediction and its applications – Part II: Life prediction of turbine blades under creep–fatigue interaction. *Int. J. Fatigue, 29*(1), 10–19.
5. Marahleh, G., Kheder, A., & Hamad, H. F. (2006). Creep life prediction of service-exposed turbine blades. *Mater. Sci. Eng. A, 433*(1-2), 305–309.
6. Kim, H.-J. (2005). Assessment of creep life fraction for in-service high-temperature components. *Eng. Fail. Anal. C., 12*(4), 578–585.
7. Maharaj, C., Morris, A., & Dear, J. P. (2012). Modelling of creep in Inconel 706 turbine disc fir-tree. *Eng. Fail. Anal., 558*, 412–421.
8. Liu, D., Li, H., & Liu, Y. (2015). Numerical Simulation of Creep Damage and Life Prediction of Superalloy Turbine Blade. *Math. Probl. Eng., 2015*(1), 1–10.
9. Shi, D., Li, Z., Yang, X., & Wang, H. (2018). Accelerated LCF-creep experimental methodology for durability life evaluation of turbine blade. *Fatigue Fract. Eng. Mater. Struct., 41*(5), 1196–1207.
10. Hyde, T. H., Sun, W., & Becker, A. A. (2005). Use of life and strain fraction rules for creep life prediction of pressurized pipe components undergoing geometry change. *J. Strain Anal. Eng., 40*(4), 385–394.
11. Raj, B., Moorthy, V., Jayakumar, T., & Rao, K. B. S. (2003). Assessment of microstructures and mechanical behaviour of metallic materials through non-destructive characterisation. *Int. Mater. Rev., 48*(5), 273–325.
12. Baby, S., Nagaraja Kowmudi, B., Omprakash, C. M., Satyanarayana, D., Balasubramaniam, K., & Kumar, V. (2008). Creep damage assessment in titanium alloy using a nonlinear ultrasonic technique. *Scripta Materialia, 59*(8), 818–821.
13. Balasubramaniam, K., Valluri, J. S., & Prakash, R. V. (2011). Creep damage characterization using a low amplitude nonlinear ultrasonic technique. *Mater. Charact., 62*(3), 275–286.
14. Ehrlich, C., Kim, J.-Y., Jacobs, L. J., Qu, J., & Wall, J. (2012). Experimental characterization of creep damage in a welded steel pipe section using a nonlinear ultrasonic technique. In *Review of Progress in Quantitative Nondestructive Evaluation, USA, VT, Burlington, 17–22 July*. (pp. 292–298, AIP Conference Proceedings): AIP.

15. Kang, J. (2000). On the Detection of Creep Damage in a Directionally Solidified Nickel Base Superalloy Using Nonlinear Ultrasound. In *AIP Conference Proceedings, Quantitative Nondestructive Evaluation, USA, Wisconsin, 27 July-1 August 2000*. (pp. 1248–1255): AIP.

16. Xiang, Y.-X., Deng, M.-X., Xuan, F.-Z., Chen, H., & Chen, D.-Y. (2012). Creep Damage Evaluation of Titanium Alloy Using Nonlinear Ultrasonic Lamb Waves. *Chin. Phys. Lett.*, *29*(10), 106202.

17. Xiang, Y., Deng, M., & Xuan, F.-Z. (2014). Creep damage characterization using nonlinear ultrasonic guided wave method: A mesoscale model. *Int. J. Appl. Phys.*, *115*(4), 44914.

18. Xiang, Y., Zhu, W., Liu, C.-J., Xuan, F.-Z., Wang, Y.-N., & Kuang, W.-C. (2015). Creep degradation characterization of titanium alloy using nonlinear ultrasonic technique. *NDT E Int.*, *72*, 41–49.

19. Valluri, J. S., Balasubramaniam, K., & Prakash, R. V. (2010). Creep damage characterization using non-linear ultrasonic techniques. *Acta Materialia*, *58*(6), 2079–2090.

20. Abdelrhman, A. M., Hee, L. M., Leong, M. S., & Al-Obaidi, S. (2015). Condition Monitoring of Blade in Turbomachinery: A Review. *Adv. Mech. Eng.*, *6*(4), 210717.

21. Burk, S. (2011). *Hochtemperaturoxidation Molybdän-basierter Legierungen unter Berücksichtigung von Einflüssen aus Umgebungsatmosphäre und legierungstechnischen Maßnahmen*. Ph.D. Thesis. University of Siegen, Siegen, Germany. (In German)

22. Obigodi-Ndjeng, G. (2011). *High Temperature Oxidation and Electrochemical Investigations on Nickel-base Alloys*. Ph.D. Thesis. University of Erlangen-Nürnberg, Erlangen, Germany.

23. Mevissen, F., & Meo, M. (2019). Detection of Cracks in Turbine Blades with Nonlinear Ultrasonic Frequency Modulation. In *Proceedings of the 12th International Workshop on Structural Health Monitoring IWSHM 2019, IWSHM 2019, Stanford, USA, 10-12 September*. (Vol. 1, pp. 824–834): DEStech Publications.

24. Mevissen, F., & Meo, M. (2020). A Nonlinear Ultrasonic Modulation Method for Crack Detection in Turbine Blades. *Aerospace*, *7*(6), 72.

25. Mevissen, F., & Meo, M. Early stage plasticity detection in gas turbine components using a nonlinear ultrasound modulation technique. *Int. J. Solids Struct.*, (Submitted).

26. Haynes International. HASTELLOY® X ALLOY. http://www.haynes.ch/doc/HASTELLOY_X.pdf. Accessed 21 April 2021.

27. Oberhauser, S. (2021). Hochtemperaturkorrosion und mögliche Abhilfemaßnahmen. https://www.wotech-technical-media.de/womag/ausgabe/2017/03/18_oberhauser_korrosion_03j2017/18_oberhauser_korrosion_03j2017.php. Accessed 30 April 2021. (In German)

28. Hikata, A., Chick, B. B., & Elbaum, C. (1965). Dislocation Contribution to the Second Harmonic Generation of Ultrasonic Waves. *J. Appl. Phys.*, *36*(1), 229–236.

29. Amura, M., Meo, M., & Amerini, F. (2011). Baseline-free estimation of residual fatigue life using a third order acoustic nonlinear parameter. *Acoust. Soc. Am.*, *130*(4), 1829–1837.

30. Malfense Fierro, G. P., & Meo, M. (2015). Residual fatigue life estimation using a nonlinear ultrasound modulation method. *Smart Mater. Struct.*, *24*(2), 25040.

31. Yost, W. T. (2000). Nonlinear ultrasonic pulsed measurements and applications to metal processing and fatigue. In *AIP Conference Proceedings, The 27th annual review of progress in quantitative nondestructive evaluation, Ames, Iowa (USA), 16-20 July 2000*. (pp. 1268–1275): AIP.

32. Cantrell, J. H., & Yost, W. T. (2001). Nonlinear ultrasonic characterization of fatigue microstructures. *Int. J. Fatigue*, *23*(SUPPL. 1), 487–490.

33. Cantrell, J. H. (2006). Quantitative Assessment of Fatigue Damage Accumulation in Wavy Slip Metals from Acoustic Harmonic Generation. *Philos. Mag.*, *86*(11).